Materials Horizons

COMMUNICATION

Published on 27 July 2026

Check for updates

Cite this: DOI: 10.1039/d6mh00868b

Received 30th April 2026,
Accepted 21st July 2026

DOI: 10.1039/d6mh00868b

rsc.li/materials-horizons

Bistability of architected metamaterials enabled by antisymmetric bending

Sibo Zhang, [a] Devin Young, [a] Dominic Vella [b] and Yunlan Zhang *[acd]

Bistable architected metamaterials exploit geometric instability to enable snap-through switching, programmable mechanical response, and reconfigurable deformation, making them attractive for soft robotics, deployable structures, and shape-morphing systems. Nevertheless, many existing bistable architected metamaterials rely on axial compression, tension, or torsion to trigger bistability. Stable state transformation triggered by an externally applied bending moment or imposed rotation remains less developed despite its natural compatibility with flexure-dominated structural systems. In addition, conventional planar bistable curved-beam unit cells provide limited geometric routes for coordinating bistability and load-bearing capacity. Here, we introduce an Antisymmetric-Bending-Enabled Architected Metamaterial (A-BEAM), a modular unit cell consisting of two three-dimensional curved shells connected by a stiff I-shaped frame. Each unit cell enables local transformation between stable states, allowing the collective response of assembled units to be translated into programmable planar and spatial reconfiguration. Stable state transformation is achieved through the antisymmetric bending deformation of the curved shells. The curved-shell geometry also provides a widthwise geometric degree of freedom for coordinating bistability and load-bearing capacity. To understand and predict this behavior, we develop a physically interpretable strip-discretized analytical model, in which the curved-shell response is constructed from the dominant bending contribution arising from strip deflection, together with strip torsion and inter-strip interactions. Experiments on 3D-printed specimens, together with finite element analysis, were used to evaluate the characteristic mechanical properties and validate the analytical model. Across the parametric FEA design space, the analytical model captures the key response features with mean relative errors of 4.9% and 9.5% for the peak moment and bistable ratio, respectively. A parametric study based on 1225 finite element simulations further shows how the mechanical behavior is primarily determined by two dimensionless geometric parameters. Compact predictive formulas are established for the peak moment and bistable ratio. Overall, the A-BEAM provides a structural strategy for developing bistable architected materials and reconfigurable systems that operate under bending, with tunable bistability and programmable shape transformation.

New concepts

This work introduces the Antisymmetric-Bending-Enabled Architected Metamaterial (A-BEAM), a modular unit cell in which stable state transformation is enabled by antisymmetric bending of three-dimensionally curved shells under an externally applied bending moment or imposed rotation. This coupling between bending load and antisymmetric curved-shell deformation is directly compatible with flexure-dominated structural systems. A key concept of this work is that the A-BEAM functions not only as an individual bistable unit cell, but also as a modular building block that can be assembled into larger reconfigurable structures. Through selective switching of local unit cells, A-BEAM assemblies can be programmed into different stable global shapes without continuous actuation, offering potential for inverse shape morphing. In addition, the three-dimensional curved-shell geometry introduces a widthwise geometric tuning route for coordinating load-bearing capacity and bistability under bending-dominated loading. Beyond the structural concept itself, the key methodological advance of this work is a physically interpretable analytical model that constructs the complex curved-shell response from strip deflection, strip torsion, and inter-strip interactions. It further enables geometry-based tuning of A-BEAM mechanical behavior, yielding compact predictive formulas for the peak moment and bistable ratio. In all, this study introduces a modular A-BEAM concept and an interpretable predictive framework for understanding, rapidly evaluating, and further developing architected metamaterials with stable state transformation under bending.

[a] *The Fariborz Maseeh Department of Civil, Architectural and Environmental Engineering, The University of Texas at Austin, TX, 78712, USA. E-mail: yunlan.zhang@austin.utexas.edu*
[b] *Mathematical Institute, University of Oxford, Woodstock Rd, Oxford, OX2 6GG, UK*
[c] *The Center for Additive Manufacturing and Design Innovation (CAMDI), The University of Texas at Austin, TX, 78712, USA*
[d] *Texas Materials Institute, The University of Texas at Austin, TX, 78712, USA*

1. Introduction

Architected metamaterials derive their mechanical properties primarily from geometry and topology rather than chemical composition. By assembling unit cells, the collective response can be programmed to exhibit a wide range of behaviors.[1,2] Among these, multistable architected metamaterials have attracted particular interest. Unlike conventional structures, multistable systems possess two or more energy minima corresponding to geometrically distinct stable configurations.[3–12] Transitions between these states can be triggered by external stimuli, while each stable configuration can be maintained without continuous actuation. This capability to access and maintain a target stable state makes multistable systems highly attractive for applications including grippers,[13–16] robotics,[17–20] energy absorption,[21–24] and vibration isolation.[25–28]

Through careful design of unit-cell geometry, topology, and materials, the mechanical behavior of multistable architected metamaterials can be systematically tailored.[2] This tunable stability makes them particularly attractive for programmable mechanical metamaterials,[21,24,29–31] reconfigurable structures,[16,20,32–34] and a wide range of advanced functional systems.[17,27,35] Among mechanical actuation modes, axial compression has been the most extensively studied, with bistable transitions achieved through buckling and snap-through in curved beams,[3–7] shells,[8–12] trusses,[36] tilted beam arrays,[37] and origami-based unit cells.[38,39] In conventional planar bistable curved-beam unit cells, however, the lack of geometric freedom in the third dimension limits the available design routes for coordinating bistability and load-bearing capacity. Beyond compression, tension-enabled bistability has also been reported, primarily through energy storage and release in prestretched linkages and kirigami-based structures.[40–42]

Compared with these axial-dominated mechanisms, torsion- and shear-driven bistability have received considerably less attention. Torsion-enabled bistability has been demonstrated in creased annuli stabilized by crease twisting,[43] in Kresling origami where panel bending and crease rotation act in concert,[44,45] and in compression–twist coupled metastructures that integrate hinged beams with Kresling-inspired trusses to achieve bistability with large collapse deformation.[46] Reprogrammable soft pneumatic metamaterials exploiting twisting bistability have further demonstrated multimodal deformation and post-fabrication tuning through modular stopper contacts.[47] Shear-enabled bistability remains even more sparsely explored, with notable examples including magnet-based periodic architectures that trap energy under end-shear loading[48] and asymmetric kirigami metamaterials that exhibit configuration switching under shear.[20]

Stable state transformation triggered by an externally applied bending moment or imposed rotation remains insufficiently explored, despite the importance of rotation and curvature in many engineering systems. This loading mode is particularly relevant to flexure-dominated systems, including grippers that lock onto objects without continuous actuation,[13,14] soft robotic arms that maintain curved configurations,[17,49] morphing wings that switch between aerodynamic profiles,[50] and deployable structures that snap into load-bearing configurations.[24] Several bending-related bistable designs have recently been reported. For example, overcurved linked conical frusta can achieve multistability through local overcurvature,[51] inflation-powered folding beams realize bistable bending through pneumatic actuation,[52] torsion–bending antagonistic actuators couple multiple deformation modes for robotic locomotion,[19] and rotational bistable mechanisms have been developed for morphing-wing applications.[50] These studies demonstrate diverse routes to bending-related bistability for reconfigurable mechanical systems. Nevertheless, modular architected unit cells that achieve bistable shape change through controllable shell deformation, while also serving as scalable building blocks for larger programmable structures, remain underexplored. In addition, conventional planar bistable curved beams provide an important foundation for bistable mechanism design, but their planar geometry limits the available design routes for coordinating bistability and load-bearing capacity. Therefore, a modular structural unit cell that is directly compatible with bending-dominated loading, provides tunable bistability, and can be assembled into programmable metamaterials is still needed.

In this paper, we propose an Antisymmetric-Bending-Enabled Architected Metamaterial (A-BEAM) unit cell composed of two three-dimensional curved shells and a stiff I-shaped frame. In the proposed A-BEAM unit cell, the externally imposed bending moment or rotation drives an antisymmetric bending deformation of the three-dimensional curved shells, which enables snap-through switching between two stable states. Unlike conventional planar bistable unit cells, the A-BEAM introduces three-dimensional geometric freedom and exhibits a tunable bistable moment–rotation (M–θ) response governed by the geometric reconfiguration of the curved shells. To understand and predict its mechanical behavior, we develop an analytical model for the curved shell. The model constructs the dominant bending contribution from the deflection of discretized strips, refines this bending description by incorporating higher-order strip modes, and further accounts for strip torsion and inter-strip interactions. The model is evaluated against experiments on ten 3D-printed ABS specimen designs and finite element analysis (FEA). Furthermore, a parametric study comprising 1225 finite element simulations is conducted over the unit cell design space to demonstrate that the mechanical behavior can be rapidly evaluated and tuned through geometric parameters, yielding compact predictive formulas for the peak moment and bistable ratio. Overall, this study integrates the A-BEAM concept, three-dimensional curved-shell geometry, and a physically interpretable analytical model, thereby providing a new route for understanding and designing bistable architected metamaterials and reconfigurable systems that operate under bending.

2. Antisymmetric-bending-enabled architected metamaterial (A-BEAM): architecture, mechanics, and analytical model

2.1. Architecture and performance metrics

An A-BEAM unit cell consists of two identical curved thin shells connected by a stiffer I-shaped frame, as shown in Fig. 1(a). The two curved shells are arranged symmetrically about the web of the frame, with their short edges clamped to the frame flanges and their long edges remaining free. Since the bistable response of each unit cell is governed primarily by the antisymmetric bending deformation of the curved shells under the imposed bending moment or rotation, the subsequent analytical modeling, parametric analysis, and performance characterization focus on a single curved shell, while the frame mainly provides boundary constraint, load transfer, and structural assembly.

Fig. 1(b) illustrates the geometric parameters of a single curved thin shell. Its geometry is defined by the length L, shell thickness t, amplitude A, and width B along the y-direction. A Cartesian coordinate system (x, y, z) is established with the center point O of the curved shell as the origin, where the reference mid-surface of the shell is described by

$$z(x,y) = -\frac{A}{2}\cos\left(\frac{2\pi x}{L}\right)\sin\left(\frac{\pi y}{B}\right), \quad x \in \left[-\frac{L}{2},\frac{L}{2}\right], \quad y \in \left[-\frac{B}{2},\frac{B}{2}\right] \tag{1}$$

The cosine term along the x-direction gives each constant-y strip a fixed–fixed curved-beam profile, which makes the geometry suitable for snap-through switching. The sine term along the y-direction makes the shell antisymmetric about the widthwise centerline $y = 0$: strips on the two sides of the centerline have opposite out-of-plane orientations while retaining smoothly varying local amplitudes. This antisymmetric

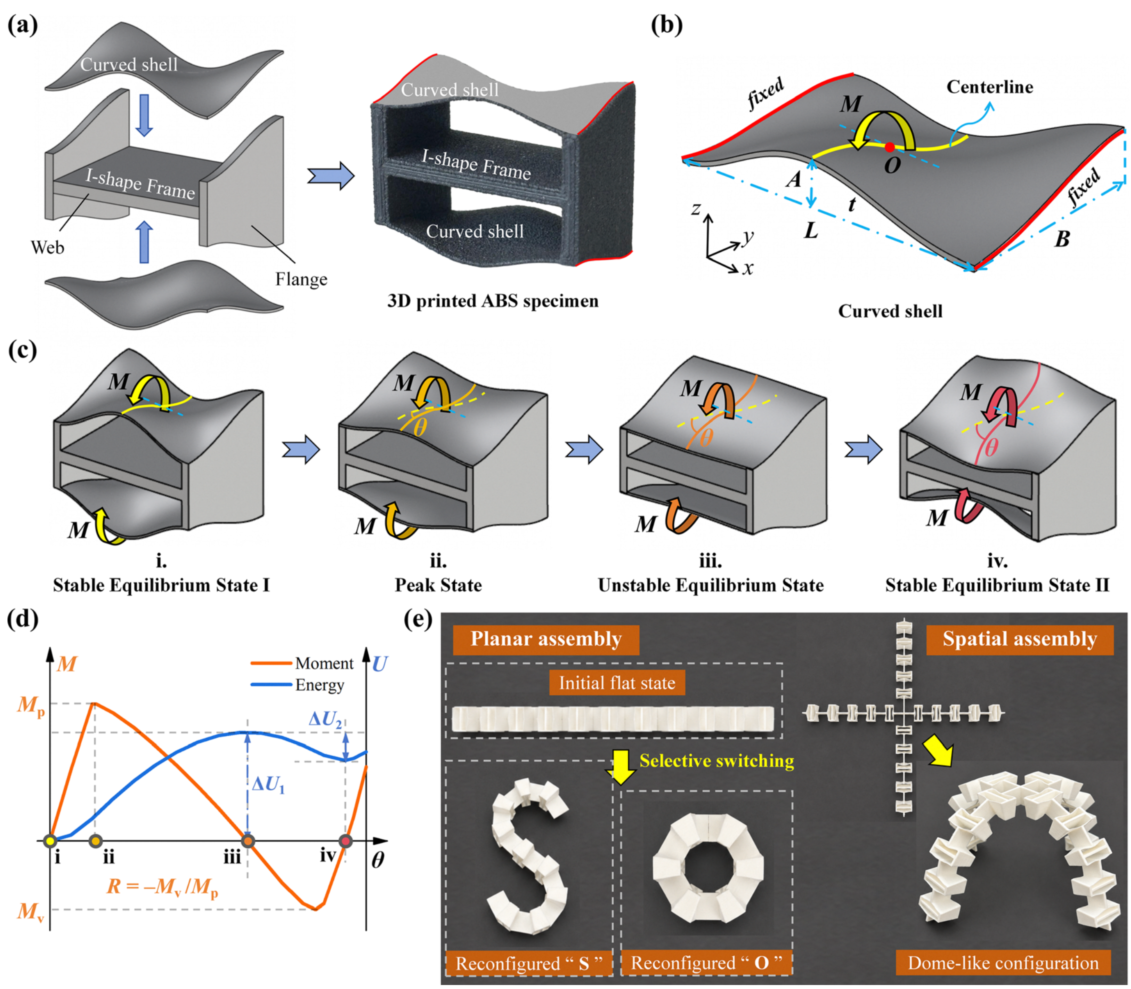

Fig. 1 Antisymmetric-bending-enabled architected metamaterial (A-BEAM) unit cell. (a) Unit cell assembly and 3D-printed ABS specimen; (b) definition of the geometric parameters, loading method, and boundary conditions of the curved shell; (c) bistable deformation process of the unit cell enabled by antisymmetric bending of the curved shells, showing four representative key states (in each of the panels ii–iv, the deformation of the centerline relative to that in panel i is highlighted); (d) characteristic moment–rotation response and its interpretation in terms of the energy landscape; (e) assembly-level demonstrations showing selective switching of A-BEAM unit-cell arrays from initially flat states into planar "S"- and "O"-shaped configurations and a spatial dome-like configuration.

curved-shell geometry is the geometric origin of the bending deformation mode that enables stable state transformation in the A-BEAM unit cell. Therefore, eqn (1) provides a curved-shell geometry with four independent design parameters, L, B, A, and t. The flange thickness of the I-shaped frame is chosen to be five times the shell thickness ($5t$), allowing the shell edges at $x = \pm L/2$ to be approximated as clamped boundaries. An external bending moment M, equivalently prescribed as an imposed rotation in the experiments and simulations, is then applied about the x-axis near the shell centerline to drive the unit cell between different stable configurations. The corresponding rotation angle θ denotes the imposed global rotation about the x-axis and is used as the generalized loading coordinate in the moment–rotation response.

Fig. 1(c) and (d) illustrates the schematic moment–rotation relationship of the unit cell under rotation-controlled loading, showing its transition between two stable configurations. Beginning from the first stable state (i), the moment increases with the applied rotation θ until it reaches the peak moment M_p at state (ii), which marks the onset of snap-through. As the rotation continues, the structure enters a negative-stiffness region with $dM/d\theta < 0$, passes through the unstable equilibrium state (iii), and finally reaches the second stable state (iv); the minimum moment observed throughout this process is defined as the valley moment, M_v. The intersections of the moment–rotation curve with the axis $M = 0$ represent equilibrium configurations: states (i) and (iv) are stable equilibria with $dM/d\theta > 0$, whereas state (iii) is an unstable equilibrium with $dM/d\theta < 0$. From an energy perspective, the blue curve in Fig. 1(d) shows the energy evolution during deformation, where the two local minima correspond to the stable equilibrium states and the local maximum corresponds to the unstable equilibrium state. The schematic energy barriers ΔU_1 and ΔU_2 illustrate the energy-landscape interpretation, and their quantitative definitions and comparison with R are provided in Section S7 of the SI.

To quantify bistability, we introduce the bistable ratio

$$R = -\frac{M_v}{M_p} \tag{2}$$

A larger positive value of R indicates a deeper negative valley moment and therefore stronger bistability. On the contrary, $R \leq 0$ indicates that the second stable configuration disappears and the structure ceases to exhibit bistability. In the following analysis, the peak moment M_p and the bistable ratio R are used as the primary metrics to characterize the mechanical behavior of the curved shell.

In addition to the moment-based bistable ratio, an energy-based metric can also be obtained by integrating the moment–rotation response along the imposed loading path. The corresponding definitions, comparison with R, and discussion of the loading-path-dependent limitation[53,54] are provided in Section S7 of the SI.

For an individual unit cell, the achievable rotation is controlled by the shell geometry. When multiple unit cells are assembled, their collective bistable transformations across stable states can generate larger overall bending angles, tunable curvature changes, and programmable global shapes. As illustrated in Fig. 1(e), an initially flat planar assembly of A-BEAM unit cells can be selectively switched into stable "S"- and "O"-shaped configurations. In addition, a spatial assembly composed of orthogonally connected A-BEAM arrays can be reconfigured into a dome-like three-dimensional structure. These demonstrations show that local stable state transformation can be translated into both global planar and spatial configurations without continuous actuation. Therefore, the A-BEAM unit cell serves not only as an individual mechanical element with tunable bistable behavior, but also as a modular building block for programmable reconfigurable structures.[51]

2.2. Development of the analytical model

To characterize the mechanical behavior of the curved shell in the proposed A-BEAM unit cell, we develop an analytical model for its moment–rotation (M–θ) relationship under quasi-static loading. As shown in Fig. 2, the curved shell is discretized into n equal strips along the width direction. This strip discretization preserves the widthwise variation of the shell geometry and describes the antisymmetric bending deformation under the imposed rotation. Based on this discretization, the overall response of the curved shell is decomposed into three components: the dominant bending contribution generated by the in-plane deflection of the discretized strips in the x–z plane (Fig. 2(a)), the torsional contribution associated with local strip rotation about the x-axis (Fig. 2(b)), and the inter-strip interaction arising from lateral mismatch between adjacent strips along the y-axis (Fig. 2(c)). Detailed derivations and implementation procedures are provided in Section S1 of the SI. For later comparison, we further distinguish a simplified isolated strip model and a final coupled strip model, whose differences are defined in part (4).

(1) Bending contribution.

As shown in Fig. 2(a), a single curved shell is discretized into n equal strips along the width (y) direction. For each discretized strip, the geometric variation along the y direction is neglected, allowing the strip to be represented by an equivalent fixed–fixed planar curved beam whose geometry is defined by the strip centerline profile. This equivalent curved beam is used to capture the bistable response generated by strip deflection along the z direction, while only its in-plane deformation in the x–z plane is considered at this stage. For the ith equivalent curved beam, f_i denotes the vertical force applied at the mid-span, and y_i denotes the effective widthwise moment arm of its center point. In this paper, n = 10, and the corresponding sensitivity analysis is presented in Section S1.3 of the SI.

Each equivalent curved beam is characterized by the span L, width $b_i = B/n$, local amplitude magnitude A_i, and thickness t. To unify the description of strip responses for different geometries, the normalized displacement is defined as $\Delta_i = d_i/A_i$, and the normalized vertical force is defined as $F_i = f_i 12L^3/(Et^3 b_i A_i)$. By adopting the model proposed in ref. 3 and retaining only the first- and third-order symmetric modes of each equivalent curved beam, explicit expressions for the normalized peak force

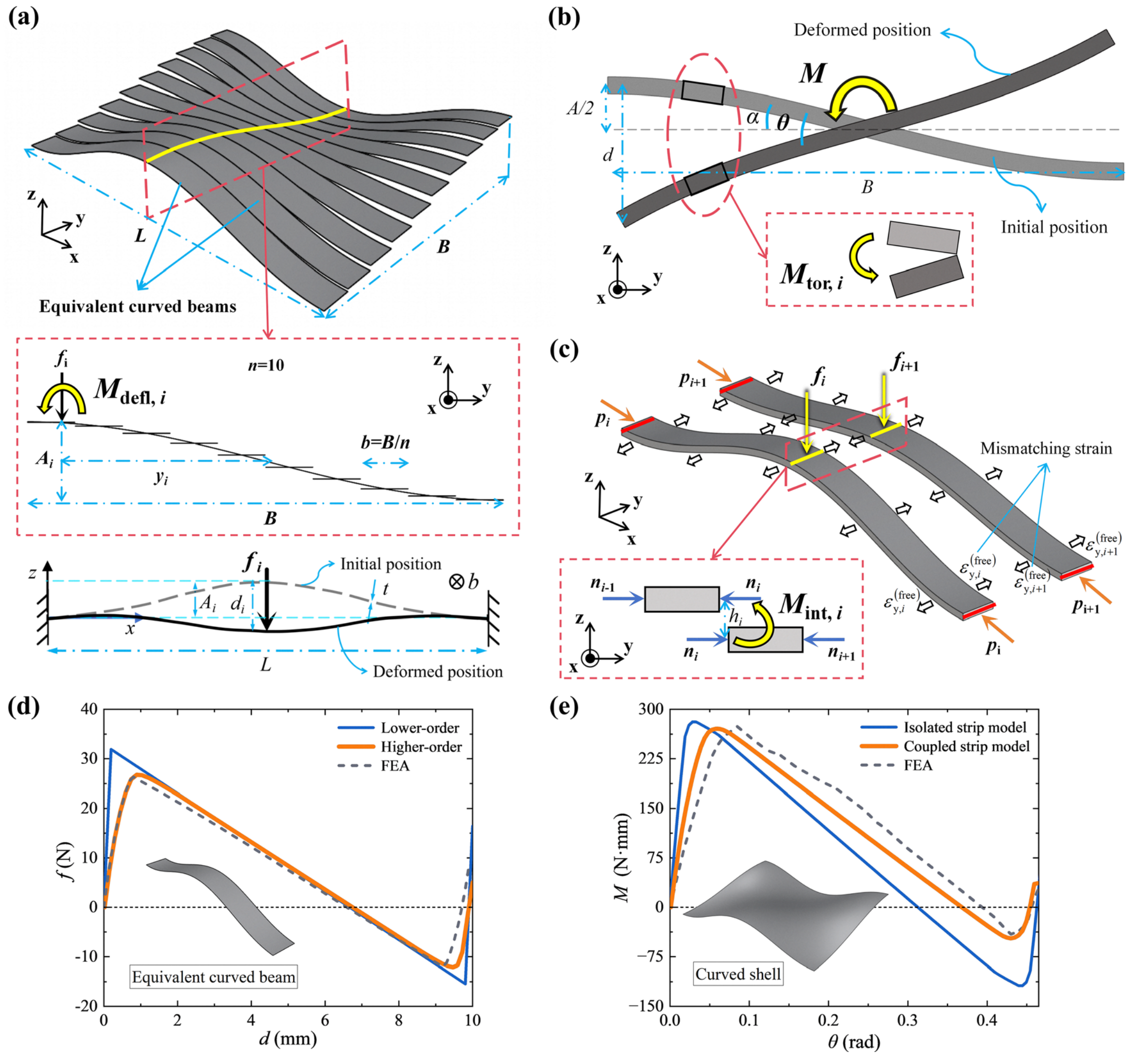

Fig. 2 Development of the analytical model for the curved shell. (a) Widthwise strip discretization and bending-moment superposition; (b) definition of the rotation angle and strip torsional contribution; (c) lateral mismatch and the resulting inter-strip interaction mechanism; (d) force–displacement response at the equivalent curved-beam level, comparing the lower-order modes description, the higher-order modes description, and the FEA result; (e) comparison of responses at the curved-shell level, showing the predictions of the isolated strip model, the coupled strip model, and the FEA result.

$F_{i,\mathrm{p}}$ and bistable ratio R_i of the equivalent curved beam can be obtained:

$$F_{i,\mathrm{p}} = 2\pi^4\left(1 + 3\sqrt{1 - \frac{16}{3Q_i^2}}\right), \quad R_i = -\frac{1 - 3\sqrt{1 - \frac{16}{3Q_i^2}}}{1 + 3\sqrt{1 - \frac{16}{3Q_i^2}}} \tag{3}$$

Here, the term symmetric modes refers to the in-plane deformation modes of each equivalent curved beam along the x-direction, whereas the full shell-level response remains governed by the widthwise antisymmetric curved-shell geometry. It can be seen that both $F_{i,\mathrm{p}}$ and R_i are determined solely by the dimensionless geometric parameter $Q_i = A_i/t$.

Fig. 2(d) compares the lower-order modes description, the higher-order modes description, and the FEA result. Here, the higher-order modes description further introduces the fifth and ninth symmetric modes on top of the lower-order one. Both descriptions are used to solve the deflection response of the equivalent curved beam, and the detailed derivations are provided in Section S1.1 of the SI. The results show that the lower-order modes description already captures the basic bistable characteristics of the equivalent curved beam, whereas the higher-order modes description improves the predictions of the peak region, valley region, and initial stiffness.

At the curved-shell level, the bending contribution $M_{(\mathrm{bend})}$ is obtained by superposing the deflection-induced moment contributions $M_{(\mathrm{defl},i)}$ of the equivalent curved beams corresponding to all strips across the width, *i.e.*,

$$M_{\mathrm{bend}}(\theta) = \sum_{i=1}^{n} M_{\mathrm{defl},i}(\theta) = \sum_{i=1}^{n} f_i(\Delta(\theta))y_i \tag{4}$$

Fig. 2(b) illustrates the centerline of the curved shell before and after deformation. The rotation angle θ is defined as the imposed rotation about the x-axis associated with the shell centerline. In the analytical model, the widthwise centerline of the curved shell is assumed to preserve its shape while rotating about the shell center. This assumption is consistent with the experimental loading method, where rotation is imposed through a stiff wall connected to the curved-shell centerline. Accordingly, the normalized displacement of the outermost strip, $\Delta_{(\mathrm{out})}$, is used as a single collective coordinate, and the strip responses are evaluated using $\Delta_i \approx \Delta_{(\mathrm{out})} = \Delta$. This approximation is most accurate for the outer strips, which dominate the total moment because of their larger amplitudes and moment arms. Further discussion is provided in Section S1.1. The relationship between Δ and the overall rotation θ can then be obtained from the outermost strip as

$$\sin(\theta - \alpha) = \frac{2}{B}\left(d - \frac{\Delta}{2}\right) = \frac{2\Delta}{B}\left(\Delta - \frac{1}{2}\right) \tag{5}$$

where α is the angle between the initial centerline of the curved shell and the horizontal line, and d is the vertical displacement of the outermost strip. Through the geometric mapping between Δ and θ, the force–displacement response of the equivalent curved beam can be converted into the moment–rotation response of the curved shell.

(2) Torsional contribution.

In the above bending contribution, each discretized strip is described only by the in-plane deflection of its corresponding equivalent curved beam in the x–z plane. However, during vertical deformation, each equivalent curved beam also undergoes local rotation about the x-axis, as illustrated in Fig. 2(b). Therefore, torsional contribution must be included, which is expressed as

$$M_{\mathrm{tor}}(\theta) = \sum_{i=1}^{n} M_{\mathrm{tor},i}(\theta) = \sum_{i=1}^{n} k_{\mathrm{tor},i}\theta \tag{6}$$

where $k_{(\mathrm{tor},i)} = 4GJ_i/S_i$ is the torsional stiffness of the ith fixed–fixed equivalent curved beam, $G = E/[2(1 + \nu)]$ is the shear modulus, J_i is the torsion constant of the curved-beam cross-section, and S_i is the arc length of the curved-beam centerline.

(3) Inter-strip interactions.

Besides bending and torsion, the overall response of the curved shell also depends on interactions between adjacent strips. As shown in Fig. 2(c), the vertical force f_i on the ith equivalent curved beam produces a beam-end axial force p_i. If the strips were analyzed in isolation, the axial force in each strip would allow it to deform laterally in the width direction according to its own response. In the continuous curved shell, however, adjacent strips remain connected, so their lateral deformations must be compatible. This compatibility requirement gives rise to an inter-strip interaction force n_i at the strip interface:

$$n_i(\Delta) = -\frac{\nu}{2}[p_{i+1}(\Delta) - p_i(\Delta)] \tag{7}$$

where ν is the Poisson ratio, which accounts for the lateral deformation associated with the axial response of each strip.

Because adjacent strips differ in geometry, they deform differently under loading. As a result, the above interaction force produces an additional moment $M_{(\mathrm{int},i)}$ at the strip interface, and its contribution to the overall bending moment can be written as

$$M_{\mathrm{int}}(\theta) = \sum_{i=1}^{n-1} M_{\mathrm{int},i}(\theta) = \sum_{i=1}^{n-1} n_i(\Delta)h_i(\Delta) \tag{8}$$

where the lever arm $h_i(\Delta)$ is defined as the average z-coordinate difference between adjacent equivalent curved beams. The detailed derivation of p_i, n_i, and h_i is provided in Section S1.2 of the SI.

(4) Decomposition of the total response.

By combining the three components described above, we obtain the final analytical model, which we call the coupled strip model. It expresses the total moment of the curved shell as

$$M^{\mathrm{coupled}}(\theta) = M_{\mathrm{bend}}^{(\mathrm{higher\text{-}modes})}(\theta) + M_{\mathrm{tor}}(\theta) + M_{\mathrm{int}}(\theta) \tag{9}$$

To gain analytical insight, we also introduce a simplified model that explicitly relates the geometric parameters to the mechanical behavior. In this isolated-strip model, strip torsion, inter-strip interactions, and higher-order mode effects are neglected. In this case,

$$M^{\mathrm{isolated}}(\theta) = M_{\mathrm{bend}}^{(\mathrm{lower\text{-}modes})}(\theta) \tag{10}$$

Fig. 2(e) compares the predictions of the isolated strip model and the coupled strip model with the FEA result. It can be seen that, although the isolated strip model captures the basic trend of the overall response, it still shows deviations in the predictions of the peak, valley, and initial stiffness. On the contrary, after incorporating the enhanced bending description, the strip torsion, and the inter-strip interactions, the coupled strip model agrees much better with the FEA result. The progressive predictions obtained by including these components are further shown in Fig. S1(d). Unless otherwise specified, the term analytical model hereafter refers to this coupled strip model. Although the model does not fully reproduce the detailed shape of the negative-stiffness regime, it captures the key mechanical metrics and bistable characteristics of the curved shell with reasonable accuracy.

2.3. Experimental and numerical assessment of the analytical model

To evaluate the analytical model established for the curved shell in Section 2.2, experiments were carried out on ten A-BEAM half-unit-cell designs with different geometric parameters. For each design, four specimens were fabricated from the same CAD geometry and tested to evaluate experimental repeatability and specimen-to-specimen variation. Their moment–rotation relationships were then compared with the predictions of the analytical model and finite element analysis (FEA). The specimen labels and geometric parameters are listed in Table S1. The specimen fabrication and experimental setup are described in Section 3.1, while the finite element (FE) modeling procedures are presented in Section 3.2.

Fig. 3(a) compares the moment–rotation (M–θ) relationship of the Base specimen obtained from experiments, FEA, and the

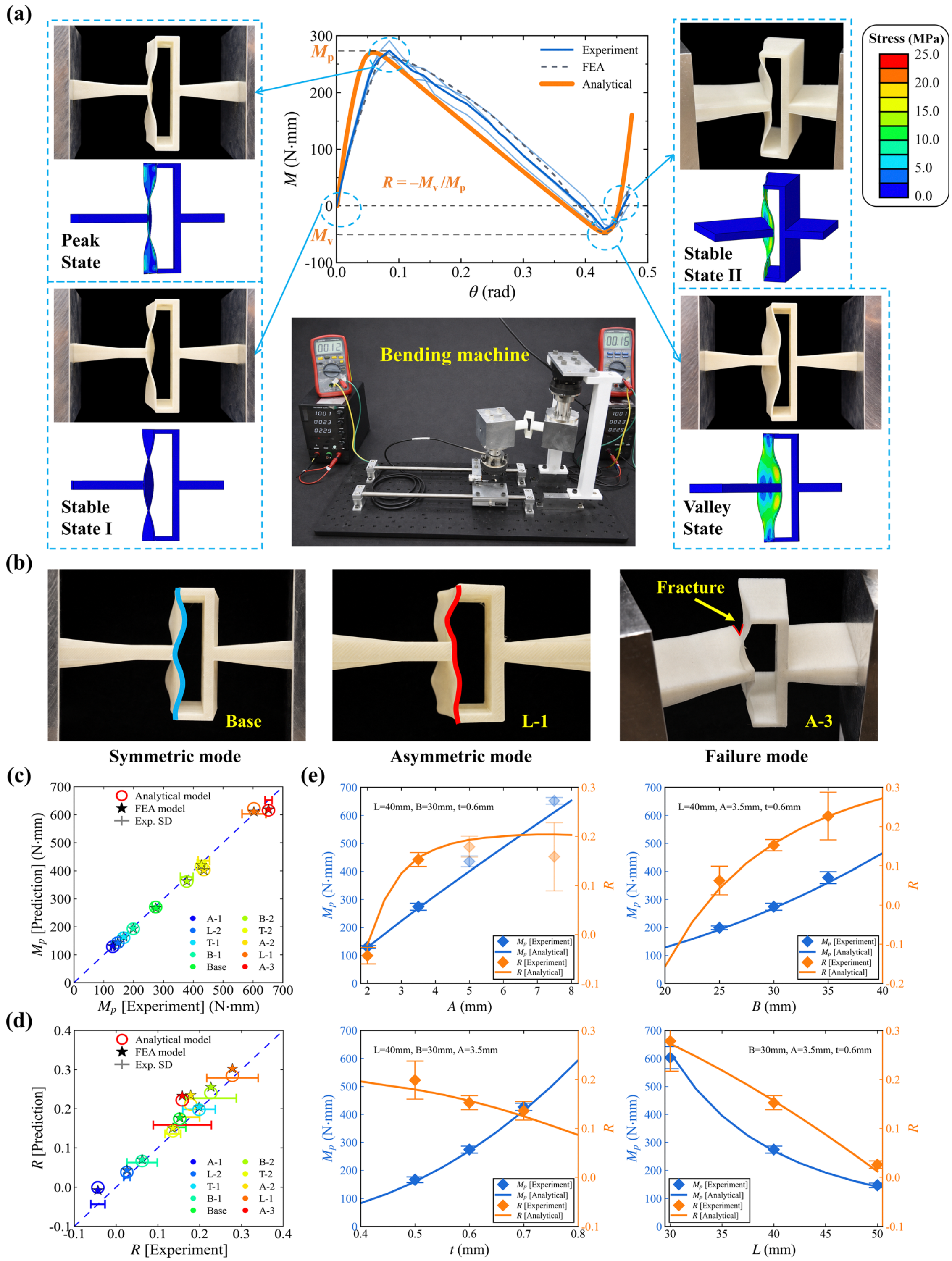

Fig. 3 Mechanical response of the curved shell and validation of the analytical model in the A-BEAM unit cell. (a) Representative moment–rotation response of the Base specimen obtained from experiments, the analytical model, and FEA, together with experimental images and FEA stress contours at characteristic states; (b) typical deformation and failure modes observed in the experiments; (c) parity plot of the peak moment M_p, comparing analytical and FEA predictions against experiments; (d) parity plot of the bistable ratio R, comparing analytical and FEA predictions against experiments; (e) experimental and analytical results showing the effects of geometric parameters on M_p and R: varying shell amplitude A with L = 40 mm, B = 30 mm, and t = 0.6 mm (top left); varying shell width B with L = 40 mm, A = 3.5 mm, and t = 0.6 mm (top right); varying shell thickness t with L = 40 mm, B = 30 mm, and A = 3.5 mm (bottom left); and varying shell length L with B = 30 mm, A = 3.5 mm, and t = 0.6 mm (bottom right). In panel (a), light blue curves denote individual repeated experiments, and the dark blue curve denotes the mean experimental response. In panels (c)–(e), experimental markers represent the mean values obtained from four repeated specimens for each specimen design, and error bars denote one standard deviation. In panel (e), lighter-colored markers indicate specimens in which fracture was observed during testing.

analytical model, while the corresponding results for the remaining specimens are provided in Fig. S2. The light blue curves denote individual repeated experiments, and the dark blue curve denotes the mean experimental response. The experimental response exhibits typical bistable behavior: the moment first increases to the peak moment M_p, after which the specimen begins to undergo evident shape reconfiguration and enters a negative-stiffness regime. During the transition from Stable State I to Stable State II, the moment decreases to the valley moment M_v, by which point the overall configurational transition is largely completed, and the response finally re-enters a positive-stiffness region. The FEA result closely reproduces the experimental response and deformation modes, while the analytical model captures the main features of the response, including the peak moment, valley moment, and overall trend. Fig. 3(c) and (d) further show that both the analytical model and FEA agree well with the experimental measurements of the peak moment and bistable ratio. The repeated experiments show that M_p is highly repeatable among specimens fabricated from the same CAD geometry, with coefficients of variation ranging from 1.8% to 6.6%. On the contrary, R exhibits larger variation because it depends on the valley moment, which is more sensitive to asymmetric transition, local damage, and fracture in thin shells. For example, the high-amplitude specimen A-3 shows a relatively large scatter in R (COV = 43.81%), consistent with the observed local fracture. For weakly bistable specimens such as B-1 and L-2, the valley moment is close to zero, so small absolute variations in M_v can lead to relatively large changes in R, with COV values of 58.11% and 28.86%, respectively. The detailed repeatability statistics are provided in the SI (Table S2).

Fig. 3(b) presents the typical deformation and failure modes observed in the experiments. Most specimens follow the intended deformation pathway of the A-BEAM unit cell. At the shell level, the deformation is governed by widthwise antisymmetric bending of the curved shell. At the strip level, the deformation of each equivalent curved beam remains dominated by symmetric in-plane modes along the x-direction, which is consistent with the assumption used in the analytical model. On the contrary, the short-length specimen L-1 and the high-amplitude specimen A-3 exhibit pronounced asymmetric modes at relatively large rotation angles, indicating a departure from the idealized deformation pathway assumed in the model. The FEA results show that high stresses are mainly concentrated in the middle region of the curved shell near its connection to the loading handle, and the experimentally observed fractures in A-3 occur in the same stress-concentrated region. These observations indicate that this transition region is a critical weak point of the curved shell and should be considered carefully in structural design. They also help explain why the analytical model predicts M_p more accurately than the valley-stage metrics. The peak moment is reached at an early loading stage, before pronounced asymmetric transition, local damage, or fracture develops. On the contrary, the valley moment and bistable ratio are determined after substantial shape reconfiguration and are therefore more sensitive to asymmetric transition, local damage, and fracture. These effects primarily influence the robustness of the second stable state rather than the initial peak load.

Fig. 3(e) summarizes the influence of geometric parameters on the peak moment M_p and bistable ratio R, where solid curves denote analytical predictions and discrete markers denote mean experimental results obtained from repeated specimens. The error bars represent one standard deviation. The results show that increasing the amplitude A and width B both increase the peak moment M_p. Increasing B also increases the bistable ratio R, whereas increasing A causes R to first increase and then gradually approach saturation. Increasing the thickness t mainly leads to a significant increase in M_p, while increasing the length L causes both M_p and R to decrease. Despite the specimen-to-specimen scatter indicated by the error bars, the mean experimental results follow the same geometry-dependent trends as the analytical predictions. Overall, the analytical model predicts the key mechanical metrics and captures the effects of geometric parameters on the curved-shell response with good accuracy.

2.4. Geometry–performance relations and predictive formulas

To better understand the mechanical behavior of the curved shell in the proposed A-BEAM unit cell over a broader parameter space and to establish predictive formulas for rapid evaluation, the relationship between geometry and mechanical response is further investigated using parametric FEA results. The parametric analysis setup is described in Section 3.3. The analytical model in Section 2.2 indicates that the local amplitude-to-thickness ratio A/t controls the bistable response of the equivalent curved-beam strips. In addition, the widthwise geometric distribution is a distinguishing feature of the present three-dimensional curved-shell architecture compared with conventional planar curved beams. Accordingly, A/t and B/L are adopted as the two dimensionless geometric parameters defining the design space. The peak moment M_p and the bistable ratio R are selected as the two primary performance metrics. An additional energy-based assessment is provided in Section S7 of the SI.

Fig. 4(a) and (b) show the distributions of the normalized peak moment (with the derivation provided in Section S4.1) and the bistable ratio in the A/t–B/L design space, respectively. In these plots, the background color represents the continuous predictions of the analytical model, while the discrete points denote the parametric FEA results. The analytical model agrees well with the FEA results across the design space, with mean relative errors of 4.9% and 9.5% for M_p and R, respectively. Fig. 4(c) further illustrates the coupled evolution of normalized peak moment and bistable ratio in the same geometric design space. The normalized peak moment increases with both A/t and B/L, indicating that a larger initial curvature and a larger width-to-length ratio both contribute to improving the load-bearing capacity of the curved shell. The bistable ratio R also exhibits a clear regional distribution. When both A/t and B/L are small, the A-BEAM unit cell tends to be monostable. As B/L increases, bistability is continuously enhanced. On the

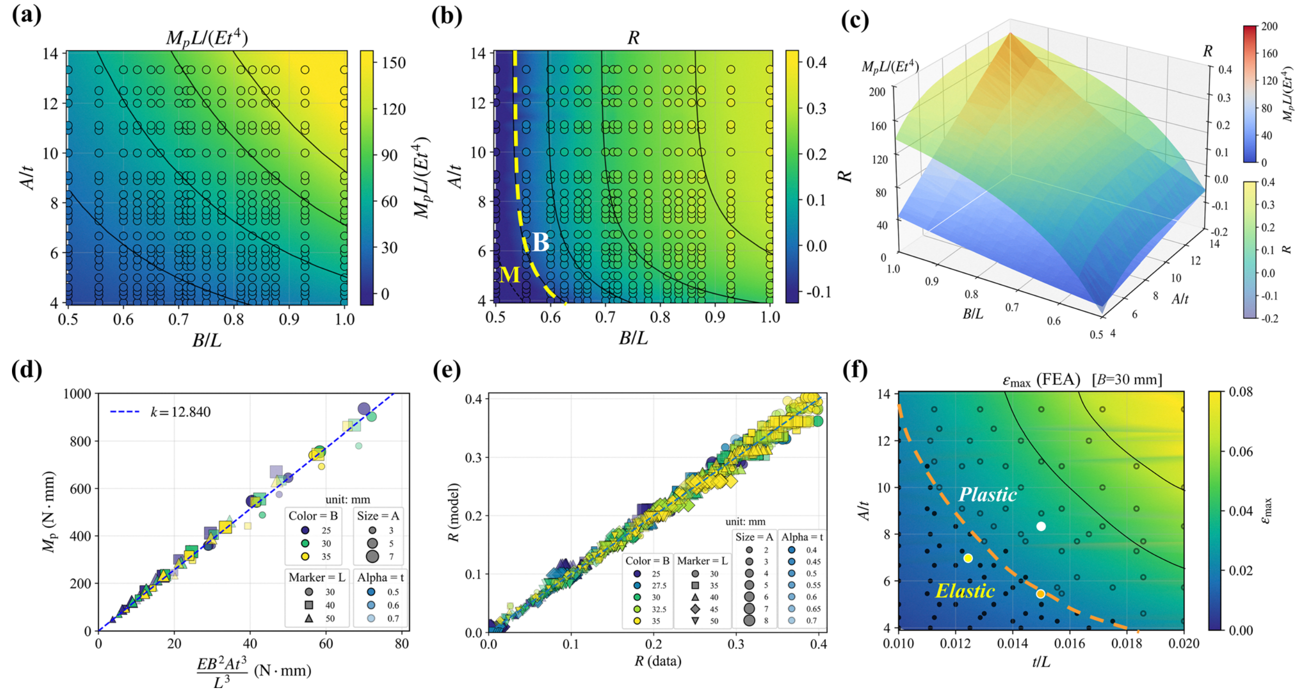

Fig. 4 Geometry–performance maps and predictive relations for the curved shell. (a) Distribution of the normalized peak moment in the A/t–B/L design space; (b) distribution of the bistable ratio R in the A/t–B/L design space, together with the R = 0 boundary separating the monostable and bistable regions; (c) coupled evolution of the normalized peak moment and bistable ratio based on the analytical model; (d) linear fitting relation for the peak moment; (e) parity plot of the predictive formula for the bistable ratio; (f) maximum-strain map from the parametric FEA results for B = 30 mm, showing the boundary between the elastic and plastic regimes. In panels (a) and (b), the background color represents the analytical prediction, while discrete points are colored according to the parametric FEA results using the same color scale. Perfect agreement between the analytical and simulation results would result in the points appearing camouflaged against the background. In panel (f), the background color represents the FEA-predicted maximum strain, where solid markers denote elastic cases and hollow markers denote cases in which plasticity occurs. The dashed orange curve indicates the approximate elastic–plastic boundary. The highlighted yellow, orange, and white markers indicate T-1, Base/B-2, and A-2, respectively, which were selected for the cyclic switching tests.

contrary, as A/t increases, bistability gradually approaches a plateau, and once A/t exceeds a certain threshold, its influence on R becomes much weaker. The R = 0 boundary is shown in Fig. 4(b) to distinguish the monostable and bistable regions.

These results reveal different roles of the two dimensionless geometric parameters in controlling the performance of the A-BEAM unit cell. Increasing A/t is highly effective in enhancing the peak moment but provides diminishing benefits for bistability beyond a certain level, whereas increasing B/L improves both load-bearing capacity and bistability. More importantly, these two features can be improved simultaneously by tuning the three-dimensional geometry of the curved shell. A representative planar curved beam is shown in the SI (Fig. S4) to illustrate the difference from an A-BEAM unit cell. Unlike the planar curved beam, the A-BEAM introduces an additional widthwise geometric tuning route, where the width-to-length ratio, B/L, can modulate bistability while also contributing to load-bearing capacity. This behavior highlights how the three-dimensional curved-shell architecture can coordinate load-bearing capacity and bistability within the investigated design space.

Based on the geometry–performance maps, compact predictive formulas are further established for the key performance metrics. In particular, the derivation in Section S4.1, based on the isolated strip model, predicts that M_p has a linear relationship with EB^2At^3/L^3, *i.e.*,

$$M_p = k_M \frac{EB^2At^3}{L^3} \tag{11}$$

This expression can be rewritten in normalized form as

$$\frac{M_pL}{Et^4} = k_M \left(\frac{A}{t}\right)\left(\frac{B}{L}\right)^2 \tag{12}$$

where k_M is a fitting coefficient. Linear fitting based on the parametric results gives k_M = 12.840, as shown in Fig. 4(d). This result indicates that the normalized peak moment can be rapidly estimated from the two dimensionless geometric parameters A/t and B/L.

In comparison, the variation of the bistable ratio R is more complex. As shown in Fig. S3(b) and S3(c), for a fixed B/L, R increases rapidly with increasing A/t at first and then gradually approaches saturation. For a fixed A/t, R exhibits an approximately linear negative correlation with $(B/L)^{-2}$. Further observations show that, when B or L is varied, the R–A/t curves differ mainly in their saturation levels, while their overall growth form remains nearly unchanged. On the contrary, when A or t is varied, the R–$(B/L)^{-2}$ curves differ mainly in their intercepts, while the slope changes only slightly. These trends suggest that the influences of A/t and B/L on R are approximately separable. Based on these observations, we propose a predictive formula for the bistable ratio:

$$R = -a\left(\frac{B}{L}\right)^{-2} + \Delta R\left[1 - \exp\left(-k_R\frac{A}{t}\right)\right] + c \quad (13)$$

where a, ΔR, k_r, and c are fitting parameters. Further details are provided in Section S4.2 of the SI.

In this expression, the first term represents the width-to-length contribution, where the negative $(B/L)^{-2}$ dependence captures the reduction of bistability at small B/L. The exponential saturation term describes the increase and subsequent saturation of bistability with increasing A/t. The parity plot in Fig. 4(e) shows that this predictive formula reproduces the parametric results well, with an average relative error of only 3.4%, thus providing a basis for rapid estimation of the bistable ratio of the curved shell. It is worth noting that the above predictive formula is intended for rapid evaluation of key performance metrics, rather than for reconstructing the complete M–θ response. In addition, because it is a fitted relation established from the FEA results within the present design space, its generalizability is more limited than that of the analytical model derived from mechanical principles.

In addition to load-bearing capacity and bistability, whether the material enters the plastic regime is also an important design constraint. Fig. 4(f) shows the distribution of the maximum strain obtained from the parametric FEA results for the case of B = 30 mm. Since the analytical model does not directly provide strain information, this map is based entirely on the FEA results. In this figure, the background color represents the maximum strain, solid markers indicate cases that remain elastic during loading, and hollow markers indicate cases that enter the plastic regime, using $\varepsilon_{\max} > 0.02$ as the criterion for the onset of plasticity. The FEA results further show that the maximum strain is governed primarily by the longitudinal strain component ε_{11} and varies only weakly with changes in B. Therefore, t/L and A/t are adopted as the horizontal and vertical coordinates, respectively, for the plasticity-boundary analysis. Fig. 4(f) thus defines the boundary between the elastically reversible region and the plastic region. It also shows that, although increasing A/t is beneficial for improving load-bearing capacity and bistability, an excessive increase may drive the structure into the plastic regime. This boundary therefore provides a direct guideline for avoiding irreversible deformation in practical applications.

To further examine how this elastic–plastic design boundary influences repeatable switching, cyclic tests were performed on four representative specimens highlighted in Fig. 4(f): T-1 in the elastic regime, Base and B-2 near the elastic–plastic boundary, and A-2 in the plastic regime. Two testing protocols were considered: ten consecutive loading–unloading cycles and five day-separated loading–unloading cycles, with a one-day interval between cycles to minimize viscoelastic effects. The detailed results are provided in Section S6 of the SI. The T-1 specimen exhibited the most stable response under both protocols, retaining approximately 95% of M_p and 90% of R after twenty continuous switches, and approximately 98% of both metrics after ten day-separated switches. Base and B-2 showed moderate degradation under continuous cycling, with M_p and R decreasing to approximately 66% and 33% for Base and 80% and 52% for B-2, respectively. Their day-separated responses remained much closer to the initial values over ten switches, with both metrics remaining above approximately 94%. As expected, the A-2 specimen, which operates in the plastic regime, exhibited rapid degradation after fracture was observed, with M_p eventually decreasing below 10% of its initial value. These results show that geometries in the elastic region are more suitable for repeatable stable state transformation, whereas geometries that enter the plastic regime are more susceptible to irreversible degradation.

3. Materials and methods

3.1. Specimen design, fabrication, and experimental methods

The test specimen represents one half of the proposed A-BEAM unit cell, consisting of one curved shell, its supporting frame, and two handles used for rotational loading. Since the bistable response of the unit cell is mainly governed by the antisymmetric bending deformation of the curved shell, and the two curved shells in the A-BEAM unit cell are arranged symmetrically about the web of the I-shaped frame, a half-unit-cell specimen was adopted to directly characterize the mechanical behavior of a single curved shell while preserving the actual boundary constraints and loading method. The geometric parameters of the specimens are listed in Table S1. Taking the Base specimen as the reference, the curved-shell amplitude A, thickness t, width B, and length L were varied separately, resulting in four groups of specimen geometries, namely the A, T, B, and L groups. Fig. 5(a) shows representative specimens with different values of L and A. For each specimen design, four specimens were fabricated from the same CAD geometry and tested. All specimens were fabricated from ABS-M30 using a Stratasys F170 FDM printer. The same build orientation and printing settings were used for all specimens to minimize process-induced variability.

The experiments were carried out using a custom-built bending machine, as shown in Fig. 5(c). The apparatus mainly consists of two rotary stages, a movable platform, and torque measurement components. The specimen was mounted by inserting the two handles into the grooves of the loading blocks on both sides, as illustrated in Fig. 5(b). This geometric matching ensured stable end connections and repeatable positioning. The two loading blocks were fixed to two rotary stages, one connected to the stationary side and the other connected to the movable platform. This arrangement ensured synchronous rotational loading at both ends while allowing the system to release redundant translational constraints during loading, thereby reducing disturbance to the target bending response of the specimen.

The experiments were conducted under rotation-controlled loading. The end rotations were synchronously imposed by the two rotary stages, and the corresponding reaction moments

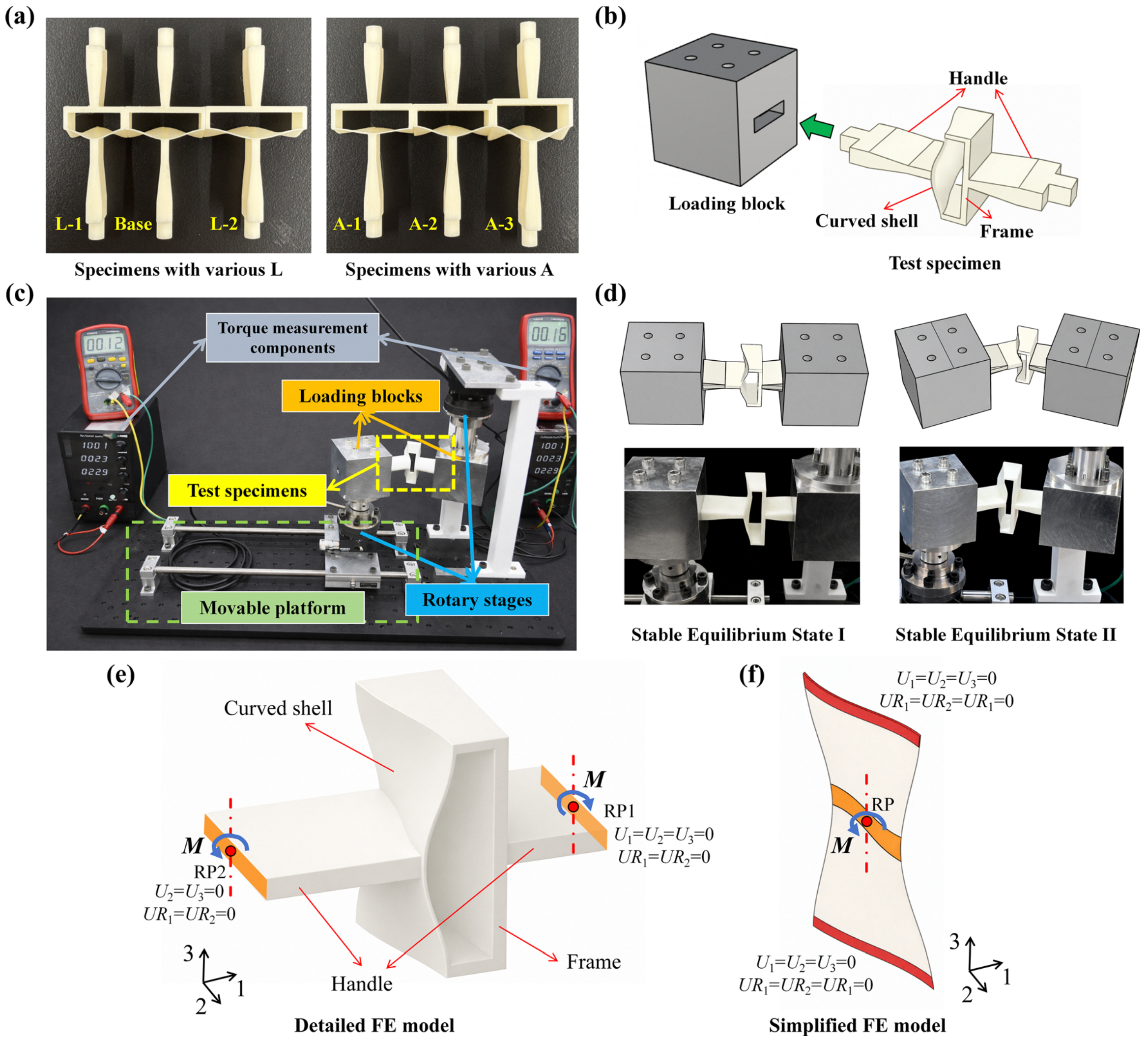

Fig. 5 Experimental setup and FE models. (a) Photos of A-BEAM half-unit-cell specimens with different shell lengths L and shell amplitudes A; (b) schematic illustration of the test specimen and the loading block; (c) custom-built rotational bending machine; (d) two stable equilibrium states observed during the experiments; (e) detailed FE model; (f) simplified shell FE model.

were recorded by the torque measurement components. These components were excited by a 10 V DC voltage, and the output voltage was converted into the corresponding moment according to the calibration results of the torque measurement components. The moment of the specimen was taken as the average of the reaction moments measured at the two rotary stages, while the global rotation angle θ was defined as the relative rotation between the two ends, corresponding to the sum of the magnitudes of the synchronously imposed end rotations. In this way, the moment–rotation response of the specimen was obtained. Fig. 5(d) shows the two stable equilibrium states observed in the experiments, at which the measured moment is close to zero.

3.2. Finite element modeling

Two finite element (FE) models were established in this work: a detailed FE model corresponding to the test specimens and a simplified shell FE model for large-scale parametric analysis. The detailed model was used to reproduce the geometry, loading method, and boundary conditions of the experimental specimens, whereas the simplified model was adopted to improve computational efficiency while retaining the dominant response mechanisms.

The detailed model is shown in Fig. 5(e), including the curved shell, the frame, and two handles used for loading. The model was discretized using C3D8R solid elements, with four elements assigned through the shell thickness to better capture bending deformation. The material properties were defined based on the tensile response of ABS-M30. The material exhibits a linear elastic response at small strains and begins to show nonlinear yielding at a strain of approximately 0.02, corresponding to a yield stress of about 33 MPa. Therefore, ε = 0.02 was used as the yield–strain threshold for identifying whether a specimen enters the plastic regime during loading.

Geometric nonlinearity was included to describe the nonlinear response under large rotation angles. The degrees of freedom of the two handle end surfaces, shown as the orange surfaces in Fig. 5(e), were coupled to two reference points, RP1 and RP2, respectively. For RP1, the translational degrees of freedom were constrained, and all rotations except the target rotational degree of freedom were suppressed. For RP2, the target rotation was prescribed, while the redundant horizontal translational degree of freedom was released to avoid over-constraining the specimen during large rotation. By extracting the reaction moments and rotation angles at the two reference points and then taking the average of the reaction moments and the sum of the rotation angles, respectively, the predicted M–θ response was obtained.

In addition to the detailed FE model used for comparison with the experiments, a simplified shell FE model was further established for parametric analysis, as shown in Fig. 5(f). This model retains only the curved shell and is discretized using S4R shell elements. Considering the thickness effects of the loading ends and boundary regions in the experiments, idealized boundary conditions were not directly imposed on the shell edges. Instead, stiffened regions were retained at the loading segment and the boundary ends, corresponding to the orange and red regions in Fig. 5(f). The nodes in these regions were coupled to reference points, at which the rotational loading and boundary conditions were applied. Compared with the detailed FE model, the simplified shell model preserves the main load-transfer characteristics and constraint effects at a significantly lower computational cost, while the discrepancy in predicting the key mechanical performance metrics remains within 5%.

3.3. Parametric analysis setup

To evaluate the variation of the mechanical behavior of the curved shell over the geometric design space, a parametric analysis was carried out based on the simplified shell FE model described in Section 3.2. In the parametric study, the shell length L was taken as 30, 35, 40, 45, and 50 mm; the shell width B was taken as 25, 27.5, 30, 32.5, and 35 mm; the shell amplitude A ranged from 2 to 8 mm with seven values in total; and the shell thickness t ranged from 0.4 to 0.7 mm with seven values in total. By combining these four geometric parameters, $5 \times 5 \times 7 \times 7 = 1225$ parametric FE models were established and analyzed, thereby covering the geometric design space considered in this work.

For each parametric model, a complete M–θ response curve was obtained under rotation-controlled loading, from which the peak moment M_p, valley moment M_v, and bistable ratio R were extracted. For the supplementary energy-barrier analysis in Section S7, the energy landscape $U(\theta)$ was calculated by numerically integrating the corresponding M–θ curve along the imposed rotation-controlled loading path. In addition, to evaluate whether the structure enters the plastic regime during loading, the maximum strain throughout the entire loading history, denoted by ε_{max}, was extracted and compared with the yield–strain threshold of 0.02.

4. Conclusions

In this work, we introduced an Antisymmetric-Bending-Enabled Architected Metamaterial (A-BEAM), whose unit cell consists of two three-dimensional curved shells connected by a stiff I-shaped frame. In this unit cell, an externally applied bending moment or imposed rotation drives the curved shells into an antisymmetric bending deformation, producing snap-through switching between two stable states. This mechanism provides a route for developing architected metamaterials that are compatible with bending-dominated structural systems. In addition, the unit cell can be assembled into planar and spatial structures, where selective switching of local unit cells enables programmable global shape reconfiguration.

To understand and predict the mechanical response of the A-BEAM unit cell, an analytical model was established for the curved shell by combining the dominant bending contribution from discretized strip deflection with strip torsion and inter-strip interactions. Experiments on ten 3D-printed specimen designs, together with finite element analysis, were used to evaluate the characteristic bistable moment–rotation response. The results show that the analytical model captures the key mechanical features of the curved shell with good accuracy, including the peak moment M_p, the bistable ratio R, and their geometry-dependent trends.

Building on this validation, a large-scale parametric study consisting of 1225 finite element models was carried out to establish geometry–performance relations over the design space. The two dimensionless geometric parameters, A/t and B/L, were found to effectively characterize the mechanical response. Increasing A/t is highly effective in enhancing the peak bending moment, whereas increasing B/L improves both the peak moment and bistability. These results show that the three-dimensional curved-shell geometry introduces a width-wise geometric tuning route for coordinating load-bearing capacity and bistability within the investigated design space. Compact predictive formulas were further established for M_p and R, enabling rapid estimation of the key performance metrics. The maximum-strain map with the elastic–plastic boundary was also established to provide a practical constraint for avoiding irreversible deformation. Overall, the proposed A-BEAM unit cell and its analytical model provide a practical basis for developing bistable architected metamaterials and reconfigurable systems that operate under bending, with tunable bistability, repeatable switching, and programmable shape transformation.

Author contributions

Sibo Zhang: writing – original draft, visualization, validation, investigation, formal analysis, data curation. Devin Young: investigation, formal analysis. Dominic Vella: writing – review & editing, writing – original draft, methodology, investigation. Yunlan Zhang: writing – review & editing, writing – original draft, supervision, resources, project administration, investigation, funding acquisition, conceptualization.

Conflicts of interest

There are no conflicts to declare.

Data availability

The data supporting this article are included in the main article and the supplementary information (SI). The SI contains analytical derivations, specimen geometries and repeatability statistics, additional experimental and finite element analysis results, a comparison with a planar curved beam, cyclic-test results, and an energy-barrier analysis. Additional data are available from the corresponding author upon reasonable request. See DOI: https://doi.org/10.1039/d6mh00868b.

Acknowledgements

This research was supported by the National University Rail Center of Excellence through a grant from the Federal Railroad Administration, U.S. Department of Transportation (grant no. 69A36524520020RRDIL). The authors also gratefully acknowledge Dr Matthew Jones for his valuable assistance during fabrication.

References

1 K. Bertoldi, V. Vitelli, J. Christensen and M. van Hecke, Flexible Mechanical Metamaterials, *Nat. Rev. Mater.*, 2017, **2**, 17066.
2 C. Zhang, X. Yin, R. Chen, K. Ju, Y. Hao, T. Wu, J. Sun, H. Yang and Y. Xu, A Review on Reprogrammable Bistable Structures, *Smart Mater. Struct.*, 2024, **33**, 093001.
3 J. Qiu, J. H. Lang and A. H. Slocum, A Curved-Beam Bistable Mechanism, *J. Microelectromech. Syst.*, 2004, **13**, 137–146.
4 X. Yao, K. Liu, Q. Dong, X. Li, C. Ma and N. Hu, Tunable and Recoverable Energy Absorption of Foam-Embedded Architected Cellular Composite Material at Multiple Strain Rates, *Compos. Struct.*, 2024, **329**, 117745.
5 W. Yan, Y. Yu and A. Mehta, Analytical Modeling for Rapid Design of Bistable Buckled Beams, *Theor. Appl. Mech. Lett.*, 2019, **9**, 264–272.
6 D. Pan, Z. Wu, F. Dai and N. Tolou, A Novel Design and Manufacturing Method for Compliant Bistable Structure with Dissipated Energy Feature, *Mater. Des.*, 2020, **196**, 109081.
7 L. Wan, D. Young, S. Zhang and Y. Zhang, Behavior of Architected Instability-Based Metamaterials (AIMs) under Out-of-Plane Geometric Variations, *Int. J. Solids Struct.*, 2026, **324**, 113682.
8 S. D. Guest and S. Pellegrino, Analytical Models for Bistable Cylindrical Shells, *Proc. R. Soc. A*, 2006, **462**, 839–854.
9 Z. Shen, C. Liu and H. Li, Viscoelastic Analysis of Bistable Composite Shells via Absolute Nodal Coordinate Formulation, *Compos. Struct.*, 2020, **248**, 112537.
10 H. Y. Meng, S. J. Zhang, Y. Zhou, Y. Q. Hou, Q. F. Chen and J. J. Jia, Snap Behaviors of Bistable Unsymmetric Cross-Ply Composite Cylindrical Shells with Different Thicknesses, *Mech. Adv. Mater. Struct.*, 2022, **29**, 6557–6566.
11 N. Vasios, B. Deng, B. Gorissen and K. Bertoldi, Universally Bistable Shells with Nonzero Gaussian Curvature for Two-Way Transition Waves, *Nat. Commun.*, 2021, **12**, 695.
12 M. Liu, L. Domino, I. D. de Dinechin, M. Taffetani and D. Vella, Snap-Induced Morphing: From a Single Bistable Shell to the Origin of Shape Bifurcation in Interacting Shells, *J. Mech. Phys. Solids*, 2023, **170**, 105116.
13 Z. Zhang, X. Ni, H. Wu, M. Sun, G. Bao, H. Wu and S. Jiang, Pneumatically Actuated Soft Gripper with Bistable Structures, *Soft Robot.*, 2022, **9**, 57–71.
14 Y. Liu, K. Luo, S. Wang, X. Song, Z. Zhang, Q. Tian and H. Hu, A Soft and Bistable Gripper with Adjustable Energy Barrier for Fast Capture in Space, *Soft Robot.*, 2023, **10**, 77–87.
15 W. Liu, X. Bai, H. Yang, R. Bao and J. Liu, Tendon Driven Bistable Origami Flexible Gripper for High-Speed Adaptive Grasping, *IEEE Rob. Automation Lett.*, 2024, **9**, 5417–5424.
16 J. He, Y. Wang, H. Tang, G. Zhang, K. Dong, D. Wang and Y. Xiong, Customizable Bistable Units for Soft-Rigid Grippers Enable Handling of Multi-Feature Objects via Data-Driven Design, *Mater. Horiz.*, 2025, **12**, 4426–4433.
17 Y. Chi, Y. Li, Y. Zhao, Y. Hong, Y. Tang and J. Yin, Bistable and Multistable Actuators for Soft Robots: Structures, Materials, and Functionalities, *Adv. Mater.*, 2022, **34**, 2110384.
18 D. K. Patel, X. Huang, Y. Luo, M. Mungekar, M. K. Jawed, L. Yao and C. Majidi, Highly Dynamic Bistable Soft Actuator for Reconfigurable Multimodal Soft Robots, *Adv. Mater. Technol.*, 2023, **8**, 2201259.
19 N. Hu, B. Li, R. Bai, K. Xie and G. Chen, A Torsion-Bending Antagonistic Bistable Actuator Enables Untethered Crawling and Swimming of Miniature Robots, *Research*, 2023, **6**, 0116.
20 C. Qiao, F. Agnelli, D. K. Pokkalla, N. D'Ambrosio and D. Pasini, Anisotropic Morphing in Bistable Kirigami through Symmetry Breaking and Geometric Frustration, *Adv. Mater.*, 2024, **36**, 2313198.
21 Y. Zhang, D. Restrepo, M. Velay-Lizancos, N. D. Mankame and P. D. Zavattieri, Energy Dissipation in Functionally Two-Dimensional Phase Transforming Cellular Materials, *Sci. Rep.*, 2019, **9**, 12581.
22 X. Yao, H. Zhao, R. Ma and N. Hu, Manipulating Localized Geometric Characteristics in Multistable Energy-Absorbing Architected Materials, *Thin Wall Struct.*, 2024, **205**, 112535.
23 W. Liu, X. Tan, S. Yan, J. Wang, H. Luo, X. Dong, T. Wen, J. Sun and J. Zhou, Multistable Metamaterials Enabled by Arched Beams for High-Efficiency Energy Absorption, *Mater. Horiz.*, 2025, **12**, 8546–8554.
24 D. Young, M. Damien, L. Wan, J. Yang and Y. Zhang, Deployable Architected Instability-Based Metamaterials through Thickness-Accommodating Kirigami Folding Method, *Mater. Des.*, 2025, **260**, 115100.
25 A. D. Shaw, S. A. Neild, D. J. Wagg, P. M. Weaver and A. Carrella, A Nonlinear Spring Mechanism Incorporating

a Bistable Composite Plate for Vibration Isolation, *J. Sound Vib.*, 2013, **332**, 6265–6275.
26 S. Ishida, H. Uchida, H. Shimosaka and I. Hagiwara, Design and Numerical Analysis of Vibration Isolators with Quasi-Zero-Stiffness Characteristics Using Bistable Foldable Structures, *J. Vibration Acoustics*, 2017, **139**, 031015.
27 Q. Zhang, D. Guo and G. Hu, Tailored Mechanical Metamaterials with Programmable Quasi-Zero-Stiffness Features for Full-Band Vibration Isolation, *Adv. Funct. Mater.*, 2021, **31**, 2101428.
28 S. Dalela, P. S. Balaji and D. P. Jena, Design of a Metastructure for Vibration Isolation with Quasi-Zero-Stiffness Characteristics Using Bistable Curved Beam, *Nonlinear Dyn.*, 2022, **108**, 1931–1971.
29 T. Chen, M. Pauly and P. M. Reis, A Reprogrammable Mechanical Metamaterial with Stable Memory, *Nature*, 2021, **589**, 386–390.
30 K. Liang, Y. Wang, Y. Luo, A. Takezawa, X. Zhang and Z. Kang, Programmable and Multistable Metamaterials Made of Precisely Tailored Bistable Cells, *Mater. Des.*, 2023, **227**, 111810.
31 J. Wu, Z. Meng, P. Li, Y. Xia, Y. Wang, M. Kadic and F. Yang, Cellular Materials with Tunable Bistability Integrating Prominent Soft and Stiff Properties, *Mater. Horiz.*, 2026, **13**, 3001–3012.
32 L. Kong and Y. F. Zhao, From Origami to Bistable and Laminate Structures: A Review for Multifunctional Applications from Structural Perspective of Shape-Changing Structures, *Adv. Intell. Syst.*, 2025, 2500505.
33 Y. Chen, J. Cai, A. Seyedkanani, A. Akbarzadeh and M. Cerruti, Strong and Flexible Graphene Oxide Paper for Humidity Responsive Origami Metamaterials, *Mater. Horiz.*, 2026, **13**, 1350–1361.
34 L. Wu, S. Chen, A. E. Acha and D. Pasini, Remorphable Architectures: Reprogramming Global Bistability through Locally Bistable Metamaterials, *Adv. Mater.*, 2026, **38**, e09940.
35 Y. Cao, M. Derakhshani, Y. Fang, G. Huang and C. Cao, Bistable Structures for Advanced Functional Systems, *Adv. Funct. Mater.*, 2021, **31**, 2106231.
36 M. Santer and S. Pellegrino, Concept and Design of a Multistable Plate Structure, *J. Mech. Design*, 2011, **133**, 081001.
37 S. Shan, S. H. Kang, J. R. Raney, P. Wang, L. Fang, F. Candido, J. A. Lewis and K. Bertoldi, Multistable Architected Materials for Trapping Elastic Strain Energy, *Adv. Mater.*, 2015, **27**, 4296–4301.
38 H. Fang, S. Li, H. Ji and K. W. Wang, Dynamics of a Bistable Miura-Origami Structure, *Phys. Rev. E*, 2017, **95**, 052211.
39 H. Fang, Y. Zhang and K. W. Wang, Origami-Based Earthworm-Like Locomotion Robots, *Bioinspiration Biomimetics*, 2017, **12**, 065003.
40 Y. Tang, Y. Chi, J. Sun, T. H. Huang, O. H. Maghsoudi, A. Spence and J. Yin, Leveraging Elastic Instabilities for Amplified Performance: Spine-Inspired High-Speed and High-Force Soft Robots, *Sci. Adv.*, 2020, **6**, eaaz6912.
41 A. Rafsanjani and D. Pasini, Bistable Auxetic Mechanical Metamaterials Inspired by Ancient Geometric Motifs, *Extreme Mech. Lett.*, 2016, **9**, 291–296.
42 X. Shang, L. Liu, A. Rafsanjani and D. Pasini, Durable Bistable Auxetics Made of Rigid Solids, *J. Mater. Res.*, 2018, **33**, 300–308.
43 T. Yu, F. Marmo, P. Cesarano and S. Adriaenssens, Continuous Modeling of Creased Annuli with Tunable Bistable and Looping Behaviors, *Proc. Natl. Acad. Sci. U. S. A.*, 2023, **120**, e2209048120.
44 Z. Zhai, Y. Wang and H. Jiang, Origami-Inspired, On-Demand Deployable and Collapsible Mechanical Metamaterials with Tunable Stiffness, *Proc. Natl. Acad. Sci. U. S. A.*, 2018, **115**, 2032–2037.
45 S. Wu, Q. Ze, J. Dai, N. Udipi, G. H. Paulino and R. Zhao, Stretchable Origami Robotic Arm with Omnidirectional Bending and Twisting, *Proc. Natl. Acad. Sci. U. S. A.*, 2021, **118**, e2110023118.
46 P. Zheng, B. Han, Z. Liu, Q. Wang, Z. Wang and Q. Zhang, Multistable Twist Metastructures with Enhanced Collapsibility and Multidimensional Programmability, *Addit. Manuf.*, 2024, **95**, 104550.
47 S. Rahman and D. Pasini, Reprogrammable Soft Pneumatic Metamaterials with Multimodal Twisting and Tunable Multistability, *Small Struct.*, 2025, **6**, 2500057.
48 X. Tan, B. Wang, K. Yao, S. Zhu, S. Chen, P. Xu, L. Wang and Y. Sun, Novel Multi-Stable Mechanical Metamaterials for Trapping Energy through Shear Deformation, *Int. J. Mech. Sci.*, 2019, **164**, 105168.
49 B. Shahryari, H. Mofatteh, A. Sargazi, A. Mirabolghasemi, D. Meger and A. Akbarzadeh, Programmable Shape-Preserving Soft Robotics Arm via Multimodal Multistability, *Adv. Funct. Mater.*, 2025, **35**, 2407651.
50 K. Barri, K. P. T. Haughn, T. C. Henry, F. R. Phillips, J. T. Hrynuk and J. Mueller, Rotational Bistable Mechanisms for Morphing Wings and Beyond, *Commun. Eng.*, 2025, **4**, 164.
51 N. P. Bende, T. Yu, N. A. Corbin, M. A. Dias, C. D. Santangelo, J. A. Hanna and R. C. Hayward, Overcurvature Induced Multistability of Linked Conical Frusta: How a 'Bendy Straw' Holds Its Shape, *Soft Matter*, 2018, **14**, 8636–8642.
52 L. J. Zhao and B. H. Sun, Bending Performance of an Inflation-Powered Bistable Folding Beam, *Eng. Struct.*, 2024, **300**, 117207.
53 G. Wan, S. J. Avis, Z. Wang, X. Wang, H. Kusumaatmaja and T. Zhang, Finding Transition State and Minimum Energy Path of Bistable Elastic Continua through Energy Landscape Explorations, *J. Mech. Phys. Solids*, 2024, **183**, 105503.
54 Q. Wang, A. Giudici, W. Huang, Y. Wang, M. Liu, S. Tawfick and D. Vella, Transient amplification of broken symmetry in elastic snap-through, *Phys. Rev. Lett.*, 2024, **132**, 267201.

